An improved method to estimate reference cloud-free images for the visible band of geostationary satellites

Florian Tornow, Nicolas Clerbaux, Alessandro Ipe & Manon Urbain

Published online: 03 Sep 2017.

Submit your article to this journal 🗗

View related articles 🗗

View Crossmark data 🗗

Taylor & Francis
Taylor & Francis Group

Check for updates

An improved method to estimate reference cloud-free images for the visible band of geostationary satellites

Florian Tornow[a,b], Nicolas Clerbaux[b], Alessandro Ipe[b] and Manon Urbain[b]

[a]Institute for Space Sciences, Freie Universität Berlin, Berlin, Germany; [b]Service Observations, Royal Meteorological Institute of Belgium, Brussels, Belgium

ABSTRACT

Geostationary images have been used frequently in the past 50 years to derive geophysical information. As a complement to all-sky observations, clear-sky counterparts play an important role in the derivation of cloud properties. We investigated ways to improve estimates of top-of-atmosphere (TOA) visible clear-sky images, over the full spatial and temporal resolution of Meteosat First Generation (MFG) satellites. Estimation was based on TOA measurements in MFG's visible channel, collected for a specific time of the day over the span of several days. In addition, a cloud climatology aided estimation.

Parameter optimization and the introduction of a spatial filter over ocean resulted in a bias of −1.0 to −2.0 digital counts (DC) and a root mean square error (RMSE) of 2.0–3.0 DC when averaged over the complete field of view. This excludes the Spring period which has up to −3.5 DC bias and up to 5.5 DC RMSE. Reasons for these exceptional differences were found in rapid greenness change, affecting reflectances over vegetated surfaces, and dust storms, with an effect over tropical land and ocean surfaces. Similarly, sea ice and snow affected polar regions seasonally. Applied to 24 years of MFG imagery, we successfully used improved clear-sky estimates to stably detect clouds. Additionally, these clear-sky estimates may prove useful for characterization of instrument degradation as well as cloud feedback studies.

1. Introduction

Observations from visible channels of weather satellites are widely used to estimate a large set of geophysical variables, such as top-of-atmosphere (TOA) and surface radiation, cloud properties, surface albedo, and many more. During daytime, the retrieval schemes often involve the use of an *a-priori* cloud-free visible image that provides an estimate of the signal that would be measured in the absence of clouds, such as in Figure 1. For example, clear-sky reflectance serves to estimate all-sky surface incident solar (SIS) radiation using the Heliosat method (e.g. Cano et al. 1986; Mueller et al. 2012). Alternatively, Ipe et al. (2003a) rely on clear-sky reflectances to identify scenes in the framework of a Geostationary Earth Radiation Budget radiance-to-flux conversion: clear-sky and instantaneous all-sky reflectance in the visible
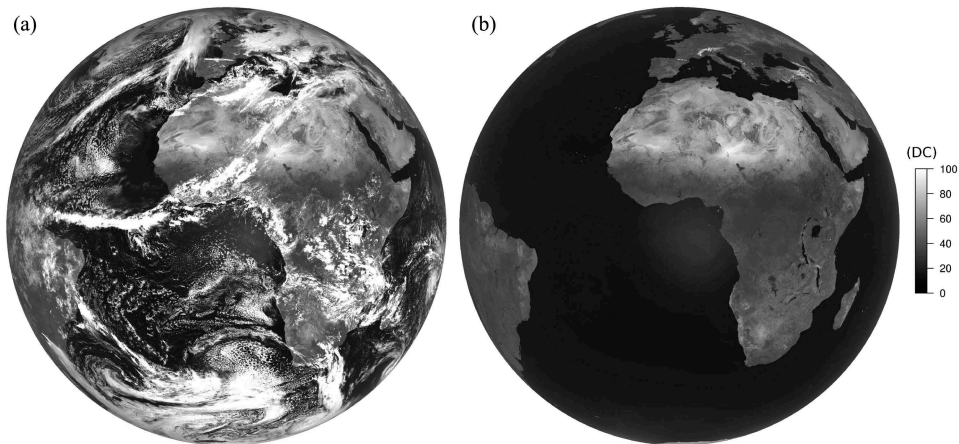
Figure 1. All-sky radiance observation (a) and desired clear-sky radiance estimate (b) in the visible band of the Meteosat Visible and InfraRed Imager (MVIRI) instrument on board the geostationary Meteosat First Generation (MFG) satellite are shown for the 02.03.2004 12:00 UTC in digital counts (DC).

channel of the Spinning Enhanced Visible and InfraRed Imager (SEVIRI) determine the cloud optical thickness. Similarly, the now-casting Satellite Applications Facility (SAF) Meteosat Second Generation (MSG) cloud mask (Derrien and Le Gléau 2005) exploits maps of clear-sky reflectance and, in contrast to previous examples, fixed monthly clear-sky maps serve as input. Likewise, Cloud Physical Properties (Roebeling, Feijt, and Stammes 2006) are based on typical clear-sky reflectances for a limited number of surface types.

In general, the cloud-free visible signal depends on the surface bi-directional reflectance, the atmospheric constituents (including water vapour and aerosols), and the Sun–target–satellite geometry. In addition, the signal changes with observing instrument calibration and spectral response curve.

For instruments on a geostationary orbit, the clear-sky estimate has often been based on a temporal analysis of the images taken over a given temporal window. To reduce the effect of the bi-directional reflectance on the signal, the analysis usually involves only images taken in the same acquisition repeat cycle of the day (hereafter referred to as *time slot*). Doing so limits the variation of the Sun–target–satellite geometry, although some change still occurs due to the Sun inclination. Additionally, this approach has the advantage of preserving the diurnal cycle from smoothing and interpolation effects. For proper processing of regions with persistent cloudiness, the extent of the temporal window has been between 30 (e.g. Posselt et al. 2012) and 60 days (Ipe et al. 2003a). For applications aiming to provide near real-time data, the window can only include days in the past (e.g. Ipe et al. 2003b). If near real time is not required (e.g. climate applications), it is better to centre the time window, to include future days as shown in the present study.

When used to derive long records of climate variables, it is important that a clear-sky estimate follows, as closely as possible, potential instrument modifications which may occur during an instrument's lifetime, e.g. calibration drift (Govaerts, Arriaga, and Schmetz 2001) or spectral response degradation (Decoster et al. 2014). An approach which follows instrument modifications has been used by the climate monitoring (CM) SAF (Schulz et al. 2009) to build the Surface Solar Radiation Data Set – Heliosat (SARAH)

product (Müller et al. 2015). The Heliosat method produces high-quality estimates of SIS radiation, even when applied to poorly calibrated instruments or in cases of doubtful instrument spectral sensitivity (Govaerts, Clerici, and Clerbaux 2004). However, ignoring instrument modification and using a static clear-sky reference could affect statistics and result in false trends of cloud fraction, as shown in Evan, Heidinger, and Vimont (2007). Processing can make use of an external cloud mask. In this case, the cloud-free signal would be estimated through the nearest-in-time observation under clear-sky conditions, as defined by the cloud mask. However, this approach may be problematic for climate applications as the resulting reference image may be affected by discontinuities in the cloud mask processing. This effect was illustrated by observed jumps and trends in several satellite data records (e.g. Wilson, Parmentier, and Jetz 2014).

To better estimate cloud-free reference images for climate applications, we have made improvements to an existing algorithm (Ipe et al. 2003a). In this article, we will show how wye optimized and validated the scheme and discuss its limitations. We will also show that the algorithm could be successfully applied to a 30+ year data set of the Meteosat visible observations and is already serving as input to processing of the Meteosat Visible and InfraRed Imager (MVIRI) and SEVIRI TOA radiation data set (Urbain et al. 2017) within the CM SAF.

2. Methodology

We will first describe how we obtained clear-sky estimates (Section 2.1) and then how we evaluated their accuracy (Section 2.2) to determine optimal parameters.

2.1. *Retrieval of clear-sky estimates*

To derive clear-sky estimates from geostationary satellites, we utilize constant observation over same locations. Focusing on one pixel in the same time slot over subsequent days, filtered radiances in the visible band

$$L^{\uparrow} = \int_{\lambda_1}^{\lambda_2} L_0^{\uparrow}(\lambda)\phi(\lambda)\mathrm{d}\lambda \tag{1}$$

(with the unfiltered radiance $L_0^{\uparrow}$, which is input to the radiometer, and the instrument's spectral response function ϕ) experience variations due to

- changing geometry between Sun, Earth, and observing satellite
- changing atmospheric conditions: the presence of clouds, aerosols, and to a lesser extent atmospheric water vapour and ozone
- changing surface parameters due to changes in vegetation, snow cover, and ocean colour
- the ageing of the instrument which modifies the spectral sensitivity $\phi(\lambda)$.

The Heliosat method aims to derive cloud albedo (*A*), necessary for the estimation of SIS, and therefore requires information on clear-sky conditions. By collecting radiances pixel wise for a specific time slot over 1 month, the maximum radiance $L_{\mathrm{max}}^{\uparrow}$ and

minimum radiance, representing the clear-sky estimate $L_{cs}^{\uparrow}$, are extracted. For an observed all-sky radiance $L^{\uparrow}$, A is computed as follows,

$$A = \frac{L^{\uparrow} - L_{cs}^{\uparrow}}{L_{max}^{\uparrow} - L_{cs}^{\uparrow}} \quad (2)$$

By using a ratio of differences of filtered radiances, ageing is taken into account. However, the method does not consider changing solar irradiance, illumination geometry, or surface parameters in order to isolate changing atmospheric conditions.

To obtain an improved estimate of filtered, clear-sky radiances, we build on the approach by Ipe et al. (2003a). As shown in Section 4, we will investigate ways to optimize the estimation in order to remove remaining cloud contaminations.

In detail, Ipe et al. (2003a) transformed digital counts (DC) into filtered radiances by using an age-respective calibration method (Govaerts, Arriaga, and Schmetz 2001). From filtered radiances, reflectances ρ_m are determined to account for a changing solar irradiation (Ipe et al. 2003a). In order to remove effects of a changing illumination geometry, a ratio of the measurement-derived all-sky reflectances ρ_m and model-derived clear-sky reflectances ρ_c over the same surface is computed. Modelled clear-sky reflectances ρ_c are based on shortwave (SW) radiances (0.3–4.0 m) collected over a panoply of viewing geometries (Loeb et al. 2003) by the Clouds and the Earths Radiant Energy System (Wielicki et al. 1996) instrument on board the Tropical Rainfall Measuring Mission satellite.

The basis for the clear-sky retrieval is a sequence of above reflectance ratios; they are collected for a window of time (61 days) and expected to vary only due to changing atmospheric conditions, leaving a cloud-free base curve and cloud-related noise contribution on top. The base curve is estimated using an assumed frequency of clear-sky conditions. Surface parameters are assumed to remain constant for the window of time.

In more detail, the sequence of reflectance ratios spans a number N of days d into the past and future around the day of interest d^* for a constant time slot t^* (e.g. 12:00 UTC). In order to estimate the clear-sky base ratio a of the day of interest, Ipe et al. (2003a) used the 5th percentile of the sequence

$$a(d^*, t^*) = \text{5th percentile of } \frac{\rho_m(d, t^*)}{\rho_c(d, t^*)} \quad \text{for } d = d^* - N, \ldots, d^*, \ldots, d^* + N \quad (3)$$

a denotes the multiplicative factor between the measurement-based reflectance, presumed to originate from clear-sky conditions, and modelled clear-sky reflectance. Thus, to derive the measurement-like clear-sky reflectance ρ_{cs}, we weight the modelled clear-sky reflectance with the estimated clear-sky base ratio

$$\rho_{cs}(d^*, t^*) = a(d^*, t^*) \times \varrho_c(d^*, t^*) \quad (4)$$

In order to reproduce an image-like product, we first transform the clear-sky reflectance into a filtered radiance $L_{cs}^{\uparrow}$

$$L_{cs}^{\uparrow}(\theta_0^*) = \frac{\rho_{cs}(d^*, t^*) \times E_0 \cos\theta_0^*}{\pi} \quad (5)$$

with θ_0^* the solar zenith angle at day d^* and time slot t^*, and E_0 the filtered solar irradiance considering Sun–Earth distance (W m^{-2}). Finally, we transform the filtered

radiance back into DC by multiplying $L_{cs}^{\uparrow}$ with the inverse of the age-dependent calibration factor.

In Section 4, we will start by examining whether the choice of N and the estimation of $a(d^*, t^*)$ are optimal.

2.2. *Evaluation of clear-sky estimates*

To select optimal parameters from a set of candidates, such as the time span length N, we need to know how accurate our clear-sky radiance estimate for each of those candidates is. To evaluate an estimated clear-sky radiance over a cloudy pixel, we would ideally know the pixels true clear-sky radiance at the exact same time.

We can act as if an actually clear region is cloudy (e.g. by setting the ratio $(\rho_m(d^*, t^*))/(\rho_c(d^*, t^*))$ to a typical cloudy value or to missing value). Subsequent estimation needs to rely on cloud-free days before and after d^*. After estimation, a cloud mask (CM SAF MSG/SEVIRI CMa [doi: http://dx.doi.org/10.5676/EUM_SAF_CM/CMA_SEVIRI/V001]) identifies clear pixels. Considering only these pixels, we compare the ignored *true* clear-sky radiances against their estimated counterparts.

In short, we knowingly turn a clear-sky pixel of the day of interest into a cloudy one, then produce a clear-sky estimate, and are able to assess the goodness of estimation when comparing the original clear-sky value against its estimate. This method, generally known as *leave-one-out cross-validation* (e.g. Theodoridis and Koutroumbas 2008), is frequently applied in parameter optimization studies and serves to select optimal parameters in Section 4.

3. Data

The following subsections present measurements from MFG's visible channel (Section 3.1) as well as a cloud climatology (Section 3.2).

3.1. *MFG visible measurements*

To apply the previously presented method and estimate TOA visible clear-sky radiances, we use TOA radiance measurements in the visible channel (0.4–1.2) of the MVIRI instrument. MVIRI has been gathering data during 1982–2006 at 0° longitude and at about 36,000 km altitude on board geostationary MFG satellites 2–7. Encoded in 8 bit count images (6 bit for MFG satellites 2–3), we downloaded the data from the European Organisation for the Exploitation of Meteorological Satellites (EUMETSAT) Data Centre.

Images cover the globe up to 80° N/S and 80° W/E over 5000 × 5000 pixels. We refer to this observable part of the globe as Meteosat Field-Of-View (FOV) or *disc*. The resolution at the sub-satellite point is about 2.5 km. Each scan took 30 min. For this study, we only used data of the 06:00, 09:00, 12:00, 15:00, and 18:00 UTC time slots during the period of February–December 2004 (MFG 7). Later, we apply the method to the full MFG archive. Apart from the above times of day, the method potentially provides visible clear-sky radiance estimates for all other time slots over Sunlit areas.

The response function of MVIRI's visible channel has a maximum at about 0.7–0.8 μm. According to Govaerts et al. (2006), the response function allows for a general sensitivity to gas absorption as well as aerosol absorption and scattering. In addition, spectral regions of fast and strong reflectance variability over vegetated areas were covered for wavelength greater 0.7 due to absorption and for below 0.7 due to scattering.

3.2. *Cloud climatology*

A cloud persistence climatology informs us about the presumed local maximum number of consecutive cloudy days. The basis of this climatology is a cloud frequency statistic over the Meteosat FOV: the International Satellite Cloud Climatology Project (ISCCP, Rossow and Schiffer 1991) D2 annual mean cloud cover. To derive cloud persistence, it is assumed that low mean cloud cover corresponds to a short persistence, and *vice versa*. Therefore, cloud persistence is translated to at least 20 and at most 60 days for lowest and highest mean cloud cover, respectively. For 50% mean cloud cover, a value of 30 days is selected. Figure 2 shows supposed maximum number of consecutive cloudy days against annual mean cloud cover. Resulting cloud persistence is mainly large over the equator and higher latitudes (see Figure 3).

4. Results

Knowledge of the clear-sky state improves estimation of SIS radiation and cloud parameters. In order to establish a reference clear-sky TOA image as counterpart to every single pixel and at each time slot of the MFG series of measurements in the visible channel, we investigated ways to optimize the approach based on the work of Ipe et al. (2003a).

Shown in Figure 4, the clear-sky estimate based on Ipe et al. (2003a) captured cloud-free conditions for most parts of the FOV. However, higher latitudes still showed signs of cloud contamination, likely arising from persistent cloudy conditions.
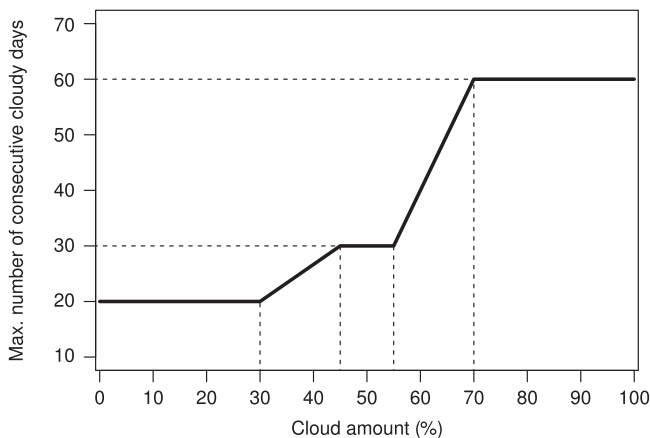

Figure 2. Assumed maximum number of consecutive cloudy days as a function of the mean ISCCP cloud cover.
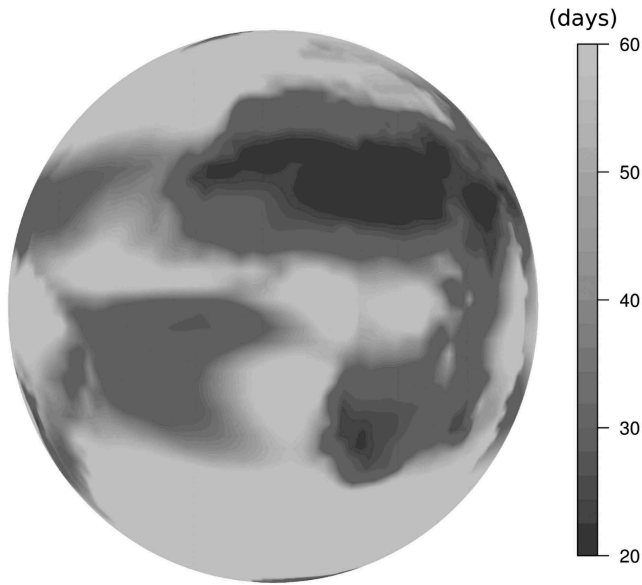
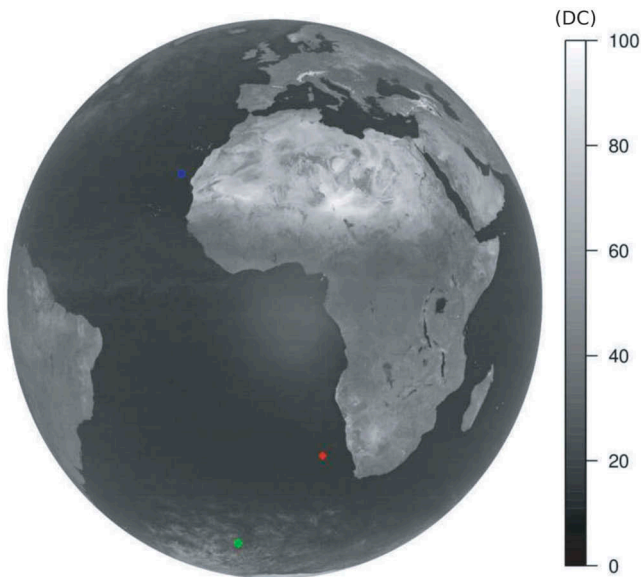**Figure 3.** Resulting cloud persistence in days.

Figure 4. Generated by using the methodology in Ipe et al. (2003a), estimated filtered TOA visible clear-sky radiances, shown in units of DC, for 12:00 UTC on 01.03.2004 contain cloud contaminated regions in higher latitudes. This study aims at providing improved clear-sky estimates. Coloured points mark pixel, which are examined further in Figure 5.

Starting from these observations, we decided to examine which choice of time span and percentile is optimal for estimation of clear-sky conditions (Section 4.1), how to handle pixels with remaining cloud contaminations (Section 4.2), which regions and
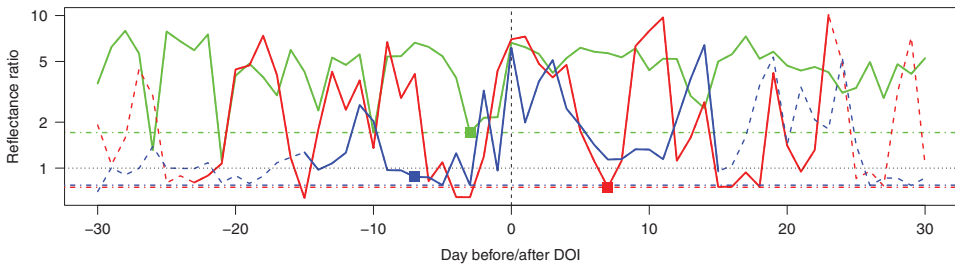
Figure 5. Reflectance ratios (shown in logarithmic scale) over subsequent days (12:00 UTC time slot), centred around the day of interest (DOI) for the 3 pixels, which are highlighted in Figure 4 (colours correspond). Solid lines show the individual, reduced time span N^*, in contrast to the full span of 30 days (broken lines). Horizontal lines indicate the 5th percentile of the full span. Squares mark the 4th lowest value of the reduces span.

times of the year remain problematic for a clear-sky estimate (Section 4.3), and, finally, verify applicability on long time series (Section 4.4). In Sections 4.1 and 4.2, we use the entire month of March 2004.

4.1. *Parameter choice*

Presented in Figure 5, reflectance ratios within the full-time span vary according to the local frequency of clouds. In mid-latitudes (blue and red), phases of expected cloud-free conditions (indicated by a ratio of about 1) happen more often than in high latitudes (green). Accordingly, the selected clear-sky estimate (the 5th percentile or, alternatively, the 4th-lowest value of ratios within the time span) is affected.

In order to capture clear conditions, an increase in time span is useful for regions with high cloud persistence. On the other hand, less cloudy regions might not benefit from longer time spans. Short-term temporal changes in surface albedo (e.g. an onset of vegetation) call for shorter time spans in order to be captured correctly.

As a solution to this dilemma, we propose using a cloud climatology (presented in Section 3.2). Knowing which areas are likely to be cloud free, we estimate clear-sky reflectances from shortened time spans. Figure 5 presents the shorter time spans through solid lines. The local number of days N^* was determined by

$$N^*(x, y) = \frac{C(x, y)}{2} \qquad (6)$$

where x and y denote the column and row value of a pixel, and $C(x, y)$ is the local value given by the cloud climatology (Figure 3).

To determine the optimal time span, we estimated cloud-free radiances using several time span lengths and compared each to clear pixels of the MFG measurement (see Figure 6). It is important to note that the estimate ignores the instantaneous value in order to mimic cloudy conditions at that time slot, where we would like to estimate radiances under clear-sky conditions as presented in Section 2.2. For frequently clear areas (triangles), any time span longer than 1 day led to good agreement with degradation beyond 10 days. Figure 6 states our assumptions: clear-sky estimates over cloud-persistent areas (circles) improved with longer time spans. A value of more than 30 days (into the past/future) did not lead to higher
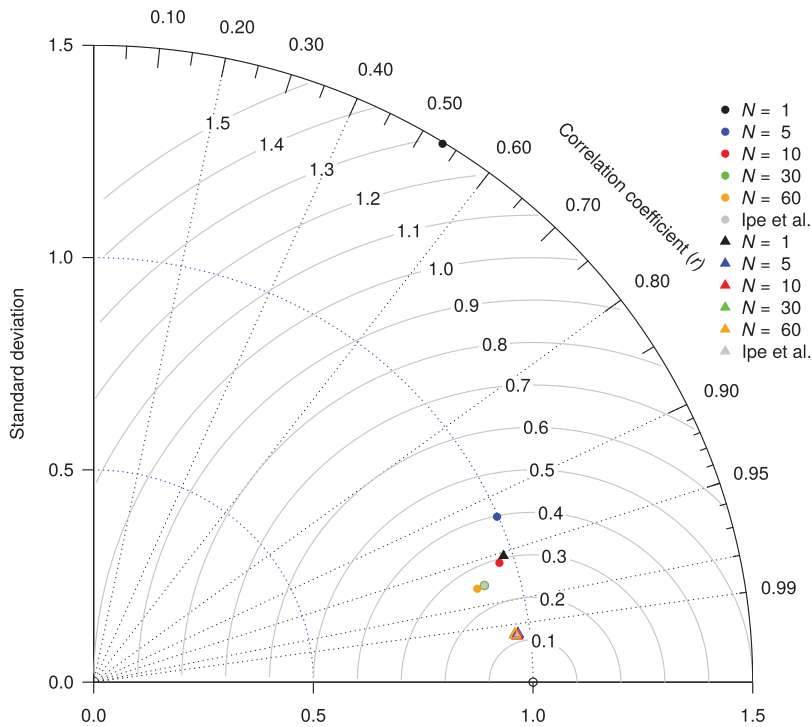
Figure 6. A Taylor diagram (Taylor 2001) allows us to select optimal parameters, here time span length. Standard deviations (SDs) (left and bottom axis) are normalized with regards to MFG radiances over cloud-free pixels, regarded as the *truth*. An estimate is entered in the diagram, according to its SD and correlation with the truth. The blue dotted line, ending and starting at 1.0, indicates how well true SD is met by estimation. The third dimension (grey circles emanating from the bottom axis) is the normalized root mean square error (RMSE). A perfect estimate would have zero RMSE, a SD of 1.0, and a correlation of 1.0 being positioned on the open circle of the bottom axis. Circles denote evaluation of frequently cloudy areas and triangles of frequently clear areas. Circle and triangle refer to the methodology of Ipe et al. 2003a.

correlation, but to a lower variability. Therefore, we consider a maximum span of 30 days into past/future (a total time span of 61 days) as the best choice to estimate clear-sky radiances.

Selecting a constant percentile from shorter time spans would imply that there are fewer values below the percentile which are expected to be lower than a relevant clear-sky candidate – such as cloud-shadow-contaminated values. For instance, the 5th percentile over the Sahara with a time span of 21 days allows just one value which is contaminated by cloud shadows. Choosing a higher percentile would be better.

As an alternative to percentiles, a uniform rank value as clear-sky estimator provides the opportunity to maintain a constant lower end for any time span. In this study, a rank r is defined as the r-lowest value X_r from a vector $\mathbf{x} \in \mathbb{R}^M$, identified from sorting

$$X_{i-1} \leq X_i, \qquad i = 2, \ldots, M \tag{7}$$

where $X_1 = \min \mathbf{x}$ and $X_M = \max \mathbf{x}$

For instance, rank 4 is greater than or equal to 3 other values in the vector, which might be too low for a clear-sky estimate.

Figure 5 compares estimation via 5th percentile over a full-time span *versus* 4th lowest rank value over a reduced time span. For these samples, it can be seen that both estimates lead to similar clear-sky ratios.

To determine which rank value provides best clear-sky values, we performed the estimation with a maximum time span of 61 days for different rank values. Figure 7 shows the performance of different estimates. Over the tropics, extra-tropical vegetated regions, and the ocean, we find highest correlations for lower rank values. However, over tropical and extra-tropical vegetation, only higher ranks provide a similarly high variability (distance to dotted blue line) of clear-sky radiances corresponding to the on- and offset of vegetation.

Over desert, higher ranks maintain a better variability. In addition, 3rd-lowest values provide a slightly lower correlation. Globally, the difference between the estimates is lower. As a trade-off between capturing variability and maintaining high correlation, the 4th-lowest rank appears as the optimal choice. In other words, each time span is expected to contain no more than 3 days which are contaminated by cloud shadows and at least 4 days which are not cloudy.

In order to ensure the best clear-sky estimation for time slots other than 12:00 UTC, we assessed different rank values for 06:00, 09:00, 15:00, and 18:00 UTC, as shown in Figure 8. As 09:00 and 15:00 UTC are estimated optimally with the rank 4, the same rank is sub-optimal for 06:00 and 18:00 UTC. Slightly better performing, higher ranks (6 and 5, respectively) are likely needed because of cloud shadow contamination, coming along with the illumination geometry.

In short, for improved clear-sky estimation, we introduced a way to reduce time span lengths of reflectance ratios where low levels of cloudiness allowed for it. We confirmed a maximum time span length of 61 days as optimal. Finally, a switch from
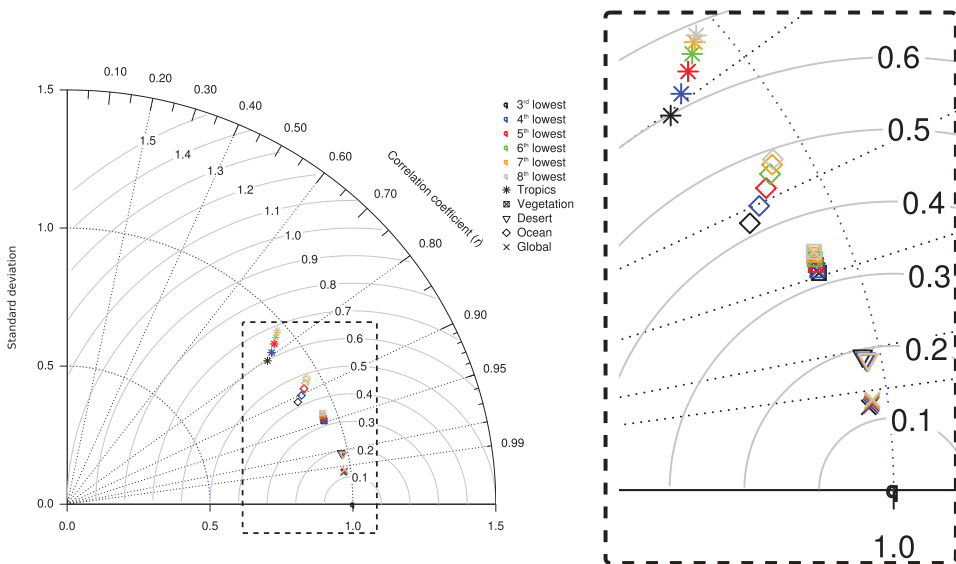

Figure 7. Similar to Figure 6, this Taylor diagram (left) allows us to select the optimal rank value for 12:00 UTC. Symbols indicate different surfaces; colours correspond to the height of the rank (e.g. blue is the 3rd lowest value out of 61 days). The rectangle is magnified on the right.
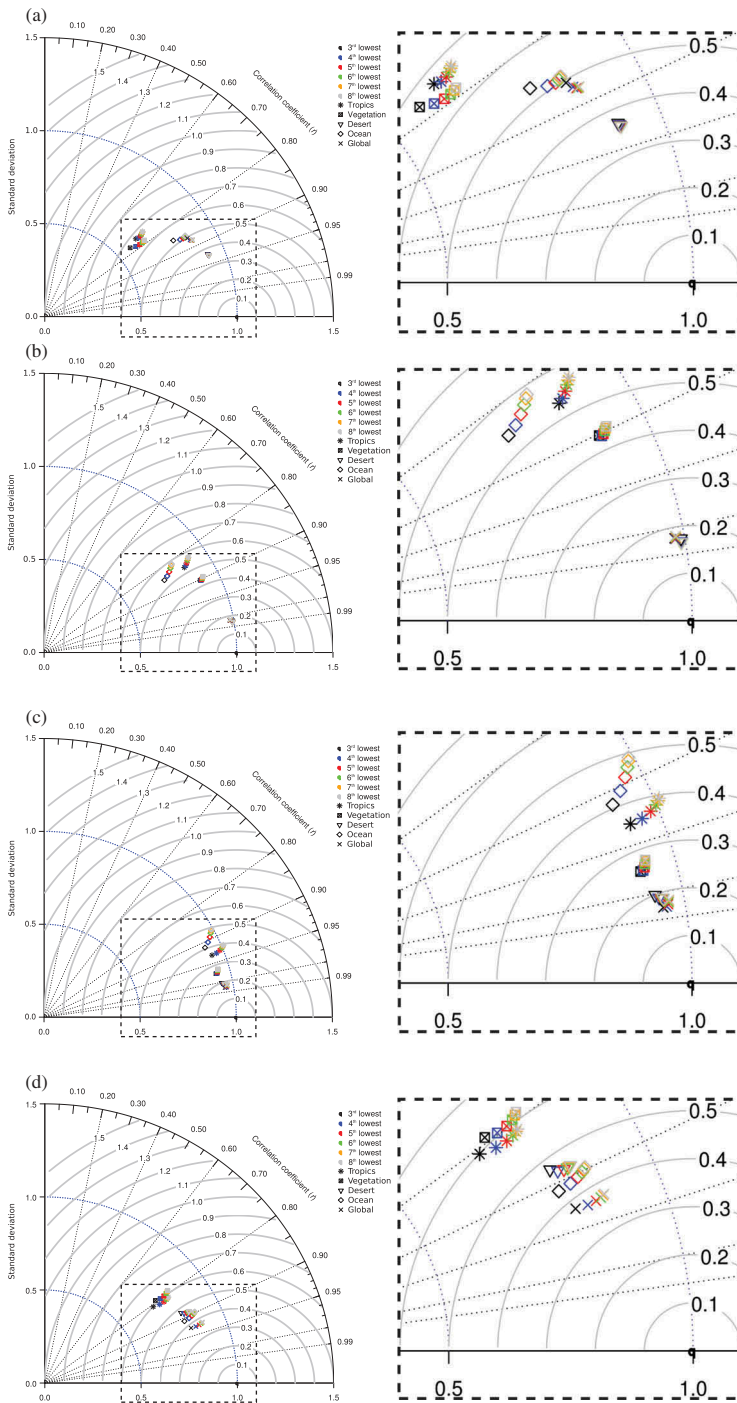
Figure 8. In addition to Figure 7, we generated clear-sky estimates for the other time slots before and after 12:00 UTC: 06:00 UTC (a), 09:00 UTC (b), 15:00 UTC (c), and 18:00 UTC (d). Generally, performance differences between rank values are rather small. For 09:00 and 15:00 UTC, 4th-lowest values present optimal rank values. However, at 06:00 UTC and 18:00 UTC, 4th lowest fail to maximize estimation performance. Higher rank values are optimal: 6th-lowest and 5th-lowest for 06:00 and 18:00 UTC, respectively. Cloud shadows likely complicate clear-sky estimation in early and late time slots.

percentiles to rank values as estimator for clear-sky base ratios proved useful, especially for shorter time spans. Optimal rank values were rank 4 and rank 5 for daytimes of low and high solar zenith angles, respectively.

4.2. Spatial filter over ocean

Parameters were optimized with regard to the full FOV. However, clear-sky estimates in higher latitudes remained cloud-contaminated. As most of these regions were located over ocean, a region of spatially homogeneous reflectances, we applied a spatial filter after estimation of clear-sky reflectances.

The idea behind the spatial filter is to select a constant number of reflectances over an ocean region, which is partly cloud contaminated. To account for a fraction of pixels with remaining cloud shadows, the 2nd percentile of this subset is assumed to resemble the clear-sky ratio. Some regions are characterized by a higher density of cloud contamination. In other words, clear-sky pixels are more scarce or further away. Instead of selecting a lower percentile over a constant region, we extended the sampling distance for areas of higher cloud persistence, keeping the percentile constant. Over usually clear ocean surfaces, on the other hand, a reduced sampling distance would be necessary to maintain local characteristics of reflectances. Again, we utilized the cloud climatology to select an individual distance Δs between samples, shown in Equation (8). Figure 9 provides an illustration of this idea.

$$\Delta s(x,y) = \begin{cases} 1 & : C(x,y) < 30 \\ 1 + \frac{12 \times (C(x,y)-30)}{30} & : 30 \leq C(x,y) \leq 60 \\ 13 & : C(x,y) > 60 \end{cases} \qquad (8)$$

In contrast to a usually dark ocean surface among bright clouds, the ocean Sun glint is characterized by a much higher reflectance. Sun glint describes specular reflection on water surfaces, usually roughened by wind-induced waves creating a distribution of tilted facets (Cox and Munk 1954). At the reflection angle equal to the incidence angle (i.e. a Sun-glint angle equals zero), chances of facets oriented such that mirror-like reflection directs Sun light to the observer are largest. In effect, reflectances are highest. In regions further away from this point (reflecting at Sun-glint angles greater zero), the chances of such facets decline and so does the reflectance. Applying the spatial filter in the vicinity of the Sun-glint spot, covering samples of brighter Sun-glint and darker non-Sun-glint pixels, and selecting the 2nd percentile would likely result in using a dark non-Sun-glint sample as a clear-sky estimate. Therefore, we adapted the percentile accordingly. Figure 10 shows the percentile as a function of Sun-glint angle.

To select the number of samples used for processing each single ocean pixel, we applied spatial filters over ocean with different grid sizes. However, the local sample distance $\Delta s(x,y)$ remained unchanged. Consequently, a larger grid size selected additional samples further away from the pixel of interest. Figure 11 shows the agreement of ocean clear-sky estimates against clear ocean pixels of the measurement. Again, leave-one-out cross-validation is applied for assessment.

Over ocean regions with short cloud persistence (squares), the best choice is no filter, although spatial filtering did eliminate some reflectance features. The next best choice is
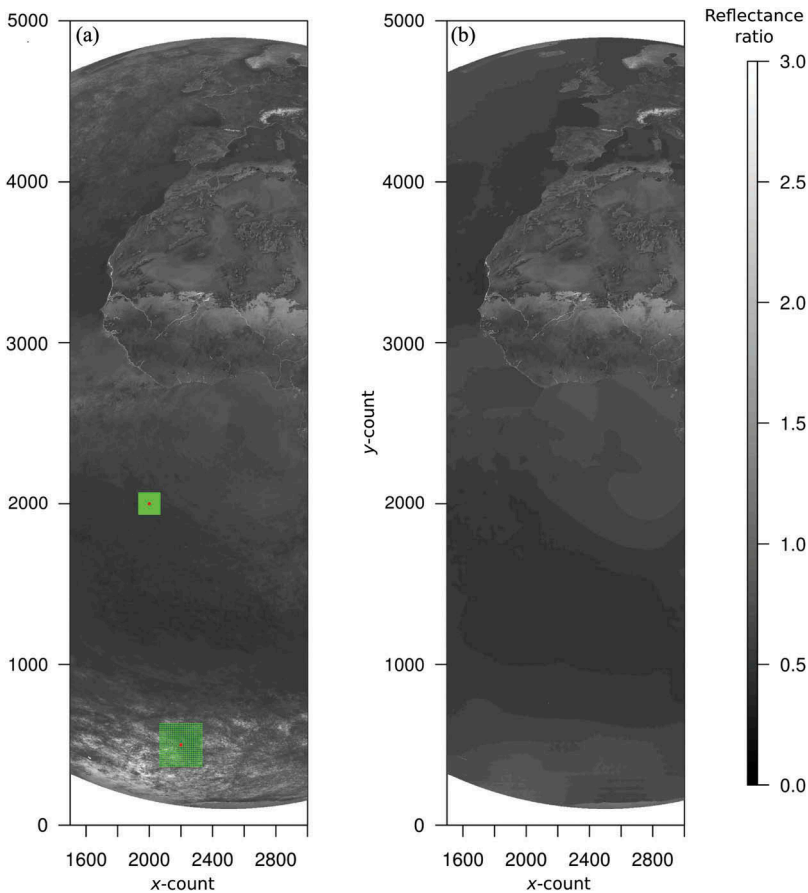
Figure 9. Shown in (a), we see estimated clear-sky reflectance ratios containing cloud contamination. *x* and *y* counts denote column and row values of each pixel, respectively. The spatial ocean filter adapts regionally with sample distance as a function of cloud persistence, as illustrated in green for two examples. As shown in (b), we see resulting reflectance ratios after filtering.
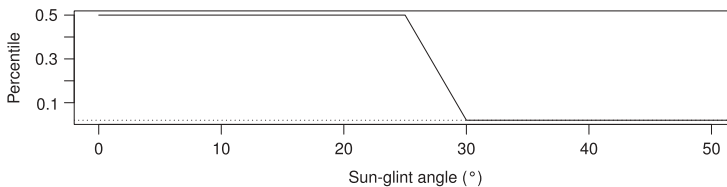

Figure 10. The plot shows the choice of percentile with regard to the Sun-glint angle of a pixel. Percentiles serve to estimate clear-sky conditions over ocean from a subset of samples, collected in the vicinity of the pixel of interest. The dotted line marks the 2nd percentile, used outside the Sun-glint region.

a filter size of 23 times 23 samples. Larger and a smaller filter size obtained slightly smaller correlations (and larger RMSE). Considering all ocean surfaces (stars), we found estimates with no filter to be closest to the variability of the measurement (dotted blue line), but to have the lowest correlations. Again, the difference in performance between
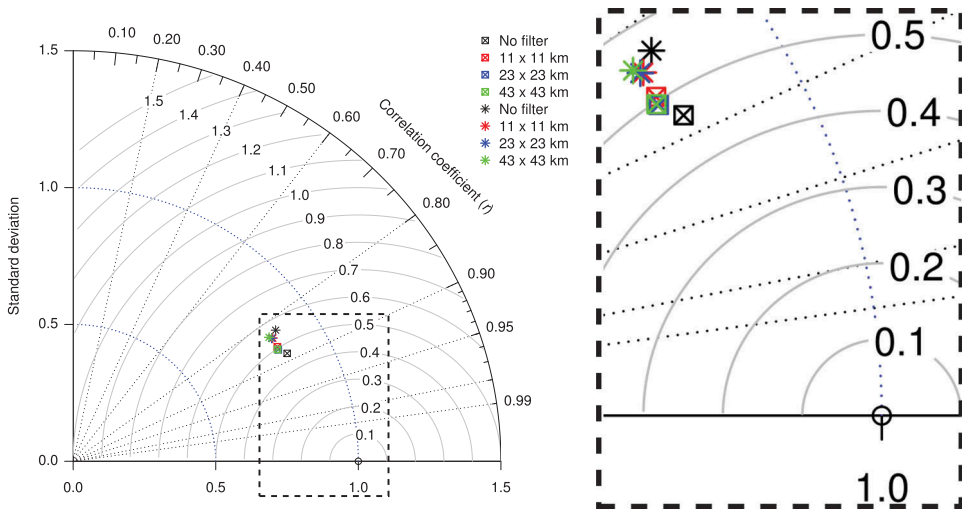
Figure 11. Similar to Figure 6, we determine the optimal sample size from this Taylor diagram. Squares indicate pixels from less cloudy ocean surfaces; stars indicate pixels of all ocean surfaces. Colours mark different sampling sizes around each pixel, corresponding to an extended grid.

different filter sizes was not large. Twenty-three times 23 samples performed as well as 11 times 11 samples. Eleven times 11, however, proved to be worse for clear ocean regions. Therefore, 23 times 23 samples represented the optimal parameter.

The clear ocean filtering is likely to suppress the higher reflectance signal in the presence of sea ice. This is a documented limitation of the method.

4.3. *Error analysis*

After optimizing parameters for TOA visible clear-sky radiance estimation with data from March 2004, we investigated estimation performance for all available months in 2004 (February until December). In contrast to Sections 4.1 and 4.2, the clear-sky estimate of this section included day d^* for estimation.

As presented in the top of Figure 12, we found all surfaces more or less steadily cloudy for the whole year: desert surfaces about 20% cloudy (yellow line) and ocean surfaces about 80% (blue line). Because of this steadiness in and outside the training month March, we expected other months to be as estimated equally well as March.

We computed bias and root mean square error (RMSE) as presented in panels (*a*) and (*b*) of Figure 12. Surprisingly, estimates in March (black lines) globally showed a stronger underestimation (bias of up to −3.0 to −4.0 DC) and larger RMSE (5.0 − 6.0 DC) than all other months (−1.0 to −2.0 DC and 2.0 − 3.0 DC, respectively). Since we already minimized error estimates for March, we assume that extraordinary circumstances complicated clear-sky radiance estimation during this month. Again split into different surfaces, vegetation (green line) and ocean surfaces contributed most to a large absolute bias (up to −5.0 DC and about −3.0 DC, respectively) and RMSE (up to 7.5 DC and about 5.0 DC, respectively) in March. We therefore suspect that there still some discrepancies caused by unstable surface parameters.
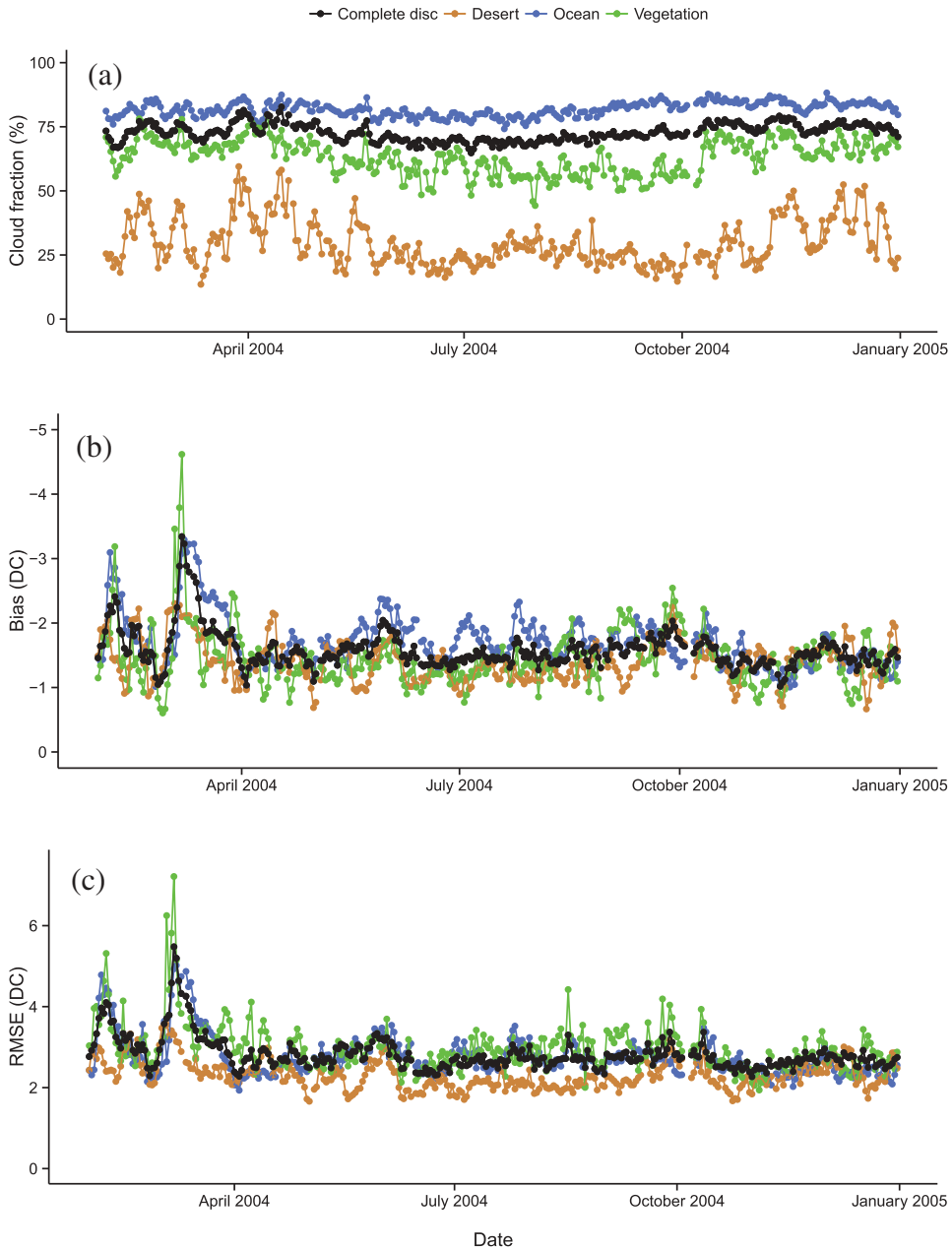
Figure 12. Cloud-free fraction (a), as well as bias (b) and RMSE (c) of estimated clear-sky radiances for February–December 2004, shown for different surface types (colours) and the full view (black).

To investigate the appearance of potentially changing surfaces, we computed the bias on seasonal maps, as presented in Figure 13. In the season of March until May, we found large areas of underestimation in Africa's tropics and western subtropics (about −2.0 to −15.0 DC). During other seasons, we underestimated less (e.g. September–November with −2.0 to −10.0 DC) or occasionally overestimated (e.g. July–August with
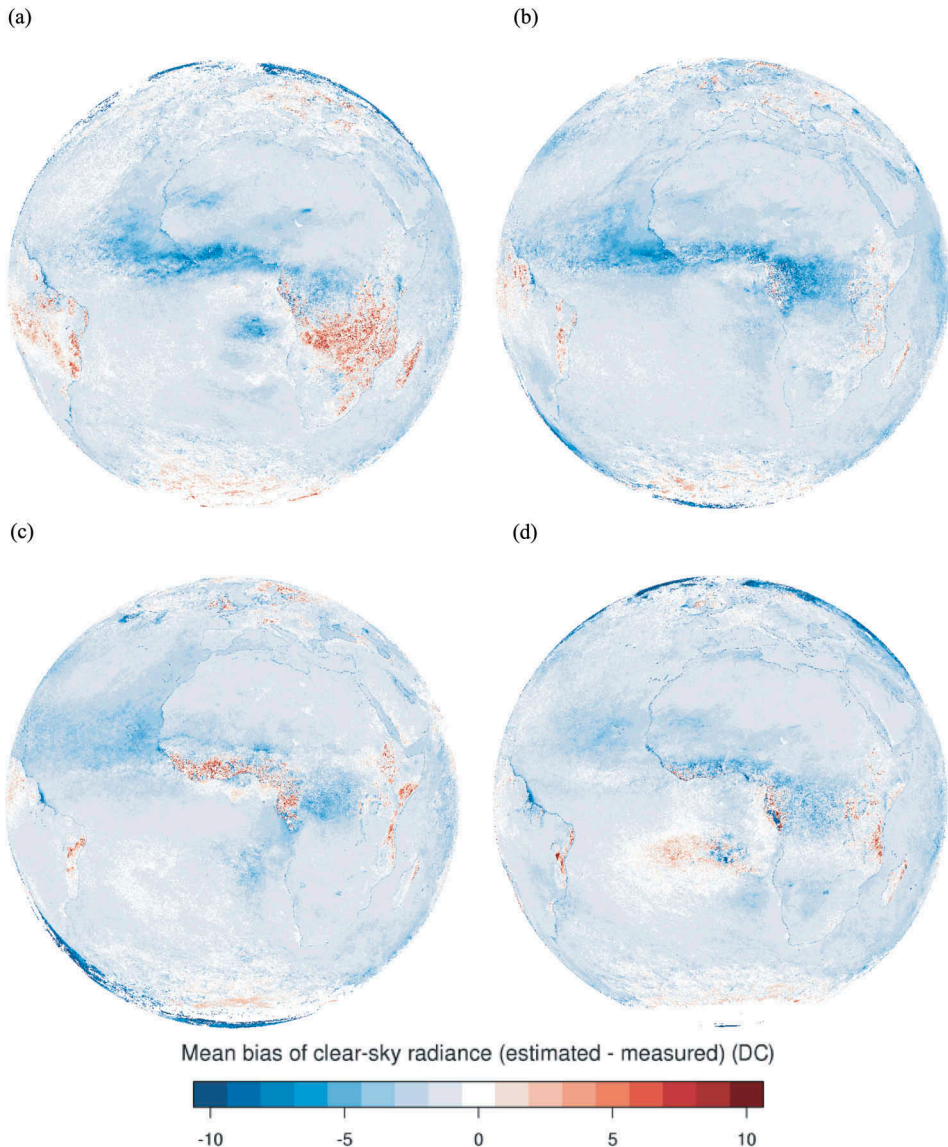
Figure 13. Seasonal plots show the bias of estimated clear-sky radiance minus MFG measurements over cloud-free areas for December and February (a), March–May (b), June–August (c), and September–November (d). Darkest colours represent differences of and beyond 10 DC.

5.0–15.0 DC) clear-sky radiances in the same area. Underestimation during December–February was potentially counterbalanced by widespread overestimation (2.0–10.0 DC) over southern Africa and Brazil. Comparing southern and western Africa and Brazil during March–May with maps on phenological transition dates based on the work of Zhang, Friedl, and Schaaf (2006), we found corresponding *onsets of greenness increase* and *onsets of greenness maximum*. We concluded that a rapid change in vegetation greenness complicated TOA SW clear-sky radiance estimation.

As this change led to both over- and underestimation, we assumed the positive and negative biases were due to the current time span position and greenness (corresponding to darkness) duration at a location. For instance, a time span covering a greenness onset right after the day of interest could bias the estimate towards the greener (hence, darker reflectance) period, resulting in an underestimate of clear-sky reflectance. On the other hand, the time span could be centred around a short period of greenness in contrast to a less green period around. This estimate would ignore the greenest (darkest) days, resulting in an overestimate of clear-sky radiance.

Clear-sky estimates over ocean surfaces (e.g. in the subtropic Atlantic) differed strongly during some seasons (March–May and December–February). We suspected dust storms were providing large areas with aerosols interacting with SW radiation, to be the reason. Based on Goudie and Middleton (2000), dust storms intensity peaks from January to June along Africa's west coast. We therefore consider dust storms as a cause for extended bias patterns over ocean.

Furthermore, polar regions had biases of up to −20.0 DC in the Arctic region for northern winter and in the Antarctic for southern winter. We suspect transient phases of sea ice and snow provide unusually bright clear-sky conditions. Similar to changing vegetation surfaces, bright phases were underestimated.

Why is there an overall negative bias? Apart from the effects mentioned, our span can naturally contain (many) more than just four clear days. Given that each clear day varies in TOA radiance due to an underlying distribution of aerosol load, captured clear days represent samples of that distribution. Facing a large number of clear days, our estimate would originate from darker conditions (i.e. the lower end of the distribution). On the other hand, given just four clear days in a span (i.e. four samples of the same distribution), we would likely estimate average conditions. We would rarely estimate a high aerosol load given any number of days and therefore rarely overestimate.

In summary, we found that optimized parameters based on March 2004 led to a global bias of −1.0 to −2.0 DC and an RMSE of 2.0–3.0 DC in estimated TOA SW clear-sky radiances for the rest of the year. Those numbers can be translated in reflectances values of −0.5% to −1% for the bias and 1–1.5% for the RMSE (100% corresponding to a perfect Lambert reflection). Seasonally pronounced biases over land together with phenology maps led to the conclusion that estimation is complicated due to a rapid change in vegetation greenness. Similarly, estimation in polar regions was prone to sea ice and snow events. Temporally underestimated clear-sky radiance over ocean surfaces were assumed to originate from Saharan dust storm events.

4.4. Evaluation of long-term application

Measured over a long period of time, TOA all-sky images are usually affected by sensor ageing in the radiometer instrument and show jumps when observed by new instruments on board follow-up satellite missions (e.g. Staylor 1990). In order to stably detect clouds in images, we aimed to generate similarly affected clear-sky counterparts. In other words, if the clear sky map fails to reproduce the instrument ageing, the ageing would reduce the fraction of detected clouds, and the retrieved cloud optical depth would decrease.

To investigate whether subsequent cloud detection works stably, we produced clear-sky images for the period February 1983–July 2006, covering Meteosat missions 2–7. Based on improved clear-sky images, we then detected clouds (Ipe et al. 2003b). We extracted estimated, clear-sky counts (daily), as well as cloud fractions (every 10 days) at the 12:00 UTC slot, averaged over the complete disk as well as separately over surface types ocean, bright vegetation, dark vegetation, bright desert, and dark desert. In addition, a monthly mean cloud fraction of daytime observations, monitored from polar-orbiting satellites (http://dx.doi.org/10.5676/EUM_SAF_CM/CLARA_AVHRR/V001), served for verification. To match Meteosat's observing geometry, we weighted geographic areas in the global data set by their representative size within the Meteosat FOV with lower weight for larger latitudes and longitudes.

Figure 14 shows clear-sky counts (coloured dots) as well as cloud fractions (grey and black dots) over time. Aside from a characteristic annual mode, clear-sky counts show an inter-annual trend within each satellite mission (i.e. each colour) which is partly offset when switched to another mission (e.g. from Meteosat 2 to 3). In addition, these trends were different between surfaces (cf. bright desert and ocean). As the spectrum of reflected solar radiance naturally varies among the surfaces, individual trends and offsets of clear-sky count suggest a spectral degradation and slightly different spectral response function, respectively, for each sensor.

In contrast to above degradations in clear-sky counts, produced cloud fraction (grey dots) emerged temporarily stable (see complete disk). However, we found long-term trends in cloud fraction (blue lines and text): over the course of the MFG period, clouds decreased about 5% in fraction at 12:00 UTC over the observable Meteosat FOV. This trend can be qualitatively confirmed using data from polar-orbiting satellites (black dots). As this data set includes observations from local sunrise to sunset, differences may occur whenever 12:00 UTC is an ill representative of daytime cloud cover. Sun et al. (2015) found similar trends over the USA.

Specific regions exhibit characteristic cloud fraction magnitude and variability (cf. dark vegetation and dark desert) as well as various long-term trends (cf. bright desert and ocean). Could these trends be a result of either missing clouds or falsely identifying clouds, caused by instrument degradation? If clouds are missed, computed clear-sky count would be contaminated with clouds and should appear brighter, while cloud fraction would be lower. If clear-sky cases are falsely identified as clouds (likely over unusually bright clear-sky pixels), less bright land pixels would contribute to the clear-sky count and cloud fraction would increase. However, we observed neither the declining cloud fraction and growing clear-sky count nor *vice versa*.

Based on cloud fraction's apparent independence from sensor degradation or sensor exchange, we conclude that derived clear-sky images are a suitable method to stably detect clouds, even when facing multi-year and multi-satellite records.

Future efforts could involve the comparison to ground-based cloud observations. Despite their small-scale applicability, the systematic errors towards detection of optically thin clouds, and a high concentration of instruments with longer time-series over the European land mass, where Meteosat's resolution is lower, ground-based instruments have the advantage of detecting clouds below satellite resolution and offer another source for stable cloud detection. The CLARA-A1 data record, which we employed for validation in this study, is based on measurements from another
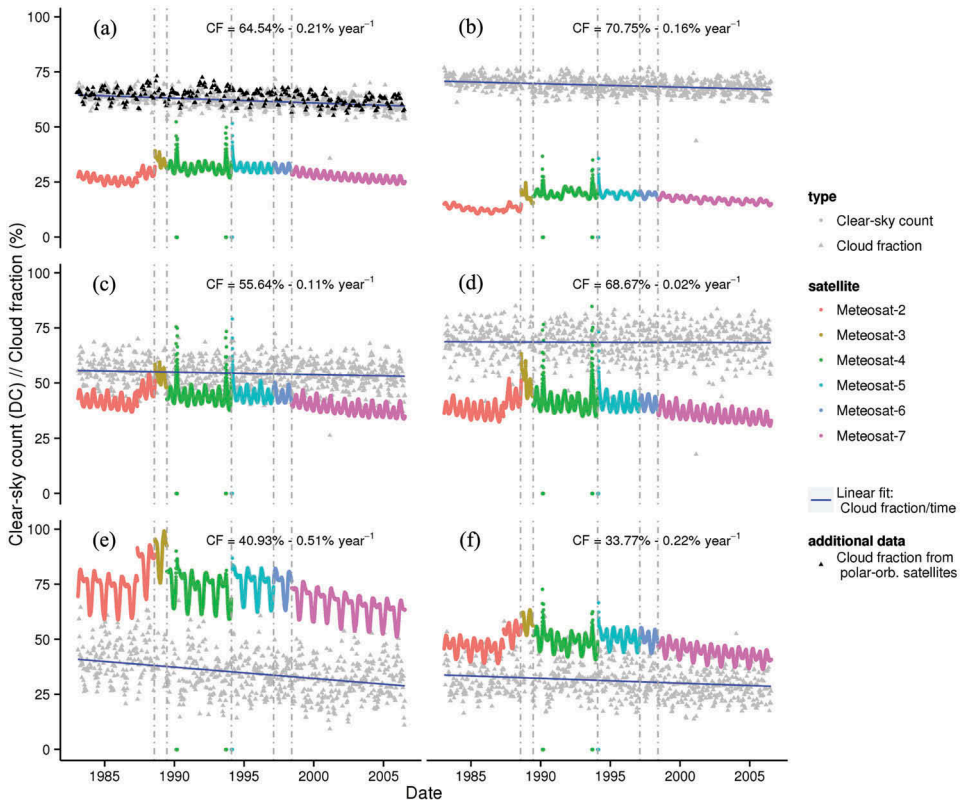
Figure 14. Shown are multi-year cloud fraction (grey/black) and clear-sky counts (coloured) aver-aged over different regions: complete disk (a), ocean (b), bright vegetation (c), dark vegetation (d), bright desert (e), and dark desert (f). Respective for each region, counts of all clear pixels on the observable disk appear daily (cloud fraction every 10 days) at 12:00 UTC. Colours indicate underlying satellites (Meteosat 2–7), and vertical lines mark each changeover. Blue lines show a linear fit of Meteosat-based cloud fraction (grey) and time (since 1983). Respective intercept and slope are shown in each upper right corner. Supplementary to Meteosat-based cloud fractions, data from polar-orbiting satellites (black) are shown as monthly daytime averages using a Meteosat-like FOV averaging. Clear-sky counts show jumps between satellites as well as long-term decay within each satellite period, likely caused by spectral response degradation. In contrast, cloud fraction remains temporally stable. Characteristic for each region is mean cloud fraction and its variability as well as detected long-term trends.

instrument (the Advanced Very High Resolution Radiometer) on board satellites with different orbit characteristics. We thus considered this record independent from the presented Meteosat retrieval and particularly suitable for comparison over the entire Meteosat disk.

5. Discussion and summary

This study aimed to estimate filtered cloud-free images from observations in the visible channel from radiometers on board geostationary satellites. We improved and validated an existing estimation approach (Ipe et al. 2003a). We showed that optimization of

parameters for statistical extraction of clear-sky features from time lines and for spatial filter over ocean surfaces resulted in a global bias of −1.0 to −2.0 DC and an RMSE of 2.0–3.0 DC for most parts of the year 2004. Larger and seasonally pronounced discrepancies over vegetated areas can be attributed to rapid changes in vegetation greenness, while dust storms presumably complicated estimation over tropical ocean surfaces. Furthermore, we show that derived cloud-free images are ideal for application to long-term records of clear-sky images for cloud detection.

Instead of assuming stable surface reflectances for estimation purposes, it seems reasonable to consider surface reflectance changes. But how do we achieve such a consideration? A possible way could be using dynamic surface maps, providing a climatology on changing parameters over surfaces due to vegetation, snow, and ice. Alternatively, vegetation changes could be detected using normalized difference vegetation index changes. As a result of such knowledge, we could reduce the time span accordingly. Future work will be directed towards the use of additional auxiliary data to account for these short-term surface changes.

We observed negative long-term trends in cloud fraction over Meteosat's observable disk. Reasons for a decreasing 12:00 UTC cloud fraction are unknown. Potentially, clouds occurred earlier or later in the day over the same location, shifted in location (i.e. out of the disk or into parts of the disk, which receive less weight when averaging), or exist less frequently in space and time. Subsequent investigations should tackle these questions.

The use of a cloud climatology for filtering clear-sky signals proved highly useful. Certainly, a monthly resolved climatology would further constrain time span length and spatial extent of the ocean filter and could, consequently, improve clear-sky image estimation.

With respect to other methods, our approach aimed at following instrument degradation as closely as possible. In addition to studying cloud and surface properties, produced cloud-free images allow investigation of instrument degradation over different surface types and may aid future calibration efforts.

References

Cano, D., J. M. Monget, M. Albuisson, H. Guillard, N. Regas, and L. Wald. 1986. "A Method for the Determination of the Global Solar Radiation from Meteorological Satellite Data." *Solar Energy* 370 (1): 31–39. ISSN 0038-092X. doi:10.1016/0038-092X(86)90104-0.

Cox, C., and W. Munk. 1954. "Measurement of the Roughness of the Sea Surface from Photographs of the Suns Glitter." *Josa* 440 (11): 838–850. ISSN 0030-3941. doi:10.1364/JOSA.44.000838.

Decoster, I., N. Clerbaux, E. Baudrez, S. Dewitte, A. Ipe, S. Nevens, A. V. Blazquez, and J. Cornelis. 2014. "Spectral Aging Model Applied to Meteosat First Generation Visible Band". *Remote Sensing* 60(3): 2534. ISSN 2072–4292. doi:10.3390/rs6032534.

Derrien, M., and H. Le Gléau. 2005. "MSG/SEVIRI Cloud Mask and Type from SAFNWC." *International Journal of Remote Sensing* 260 (21): 4707–4732. ISSN 0143-1161. doi:10.1080/01431160500166128.

Evan, A. T., A. K. Heidinger, and D. J. Vimont. 2007. "Arguments against a Physical Long-Term Trend in Global ISCCP Cloud Amounts." *Geophysical Research Letters* 340 (4): L04701. doi:10.1029/2006GL028083. ISSN 1944-8007.

Goudie, A., and N. Middleton. 2000. "Saharan Dust Storms: Nature and Consequences." *Earth-Science Reviews* 560 (1–4): 179–204. ISSN 0012-8252. doi:10.1016/S0012-8252(01)00067-8.

Govaerts, Y., A. Arriaga, and J. Schmetz. 2001. "Operational Vicarious Calibration of the MSG/SEVIRI Solar Channels." *Advances in Space Research* 280 (1): 21–30. ISSN 0273-1177. doi:10.1016/S0273-1177(01)00269-1.

Govaerts, Y., B. Pinty, M. Taberner, and A. Lattanzio. 2006. "Spectral Conversion of Surface Albedo Derived from Meteosat First Generation Observations." *IEEE Geoscience and Remote Sensing Letters* 30 (1): 23–27. ISSN 1545-598X. doi:10.1109/LGRS.2005.854202.

Govaerts, Y., M. Clerici, and N. Clerbaux. 2004. "Operational Calibration of the Meteosat Radiometer VIS Band." *Geoscience and Remote Sensing, IEEE Transactions On* 420 (9): 1900–1914. ISSN 0196-2892. doi:10.1109/TGRS.2004.831882.

Ipe, A., C. Bertrand, N. Clerbaux, S. Dewitte, L. Gonzalez, and B. Nicula. 2003b. "Validation and Homogenization of Cloud Properties Retrievals for RMIB GERB/SEVIRI Scene Identification." *SPIE Proceedings* 4882: 29–39. doi:10.1117/12.462419.

Ipe, A., N. Clerbaux, C. Bertrand, S. Dewitte, and L. Gonzalez. 2003a. Pixel-Scale Composite Top-Of-The-Atmosphere Clear-Sky Reflectances for Meteosat-7 Visible Data. *Journal of Geophysical Research* 1080(D19). ISSN 0148-0227. 10.1029/2002JD002771

Loeb, N., N. Manalo-Smith, S. Kato, W. F. Miller, S. K. Gupta, P. Minnis, and B. A. Wielicki. 2003. "Angular Distribution Models for Top-of-Atmosphere Radiative Flux Estimation from the Clouds and the Earths Radiant Energy System Instrument on the Tropical Rainfall Measuring Mission Satellite. Part I: Methodology." *Journal of Applied Meteorology* 420 (2): 240–265. February. ISSN 0894-8763. doi:10.1175/1520-0450(2003)042<0240:ADMFTO>2.0.CO;2.

Mueller, R., T. Behrendt, A. Hammer, and A. Kemper. 2012. "A New Algorithm for the Satellite-Based Retrieval of Solar Surface Irradiance in Spectral Bands." *Remote Sensing* 40 (3): 622–647. ISSN 2072-4292. doi:10.3390/rs4030622.

Müller, R., U. Pfeifroth, C. Träger-Chatterjee, R. Cremer, J. Trentmann, and R. Hollmann. 2015. *Surface Solar Radiation Data Set - Heliosat (SARAH), 1st ed. Satellite Application Facility on Climate Monitoring.* doi: 10.5676/EUM_SAF_CM/SARAH/V001.

Posselt, R., R. Mueller, R. Stöckli, and J. Trentmann. 2012. "Remote Sensing of Solar Surface Radiation for Climate Monitoring the CM-SAF Retrieval in International Comparison". *Remote Sensing of Environment* 118: 186–198. March. ISSN 0034-4257. 10.1016/j.rse.2011.11.016

Roebeling, R. A., A. J. Feijt, and P. Stammes. 2006. "Cloud Property Retrievals for Climate Monitoring: Implications of Differences between Spinning Enhanced Visible and Infrared Imager (SEVIRI) on METEOSAT-8 and Advanced Very High Resolution Radiometer (AVHRR) on NOAA-17." *Journal of Geophysical Research: Atmospheres* 1110 (D20): 1–16. ISSN 2156-2202. doi:10.1029/2005JD006990.

Rossow, W. B., and R. A. Schiffer. 1991. "ISCCP Cloud Data Products." *Bulletin of the American Meteorological Society* 720 (1): 2–20. ISSN 0003-0007. doi:10.1175/1520-0477(1991)072<0002:ICDP>2.0.CO;2.

Schulz, J., P. Albert, H.-D. Behr, D. Caprion, H. Deneke, S. Dewitte, B. Duerr, et al. 2009. "Operational Climate Monitoring from Space: The EUMETSAT Satellite Application Facility on Climate Monitoring (CM-SAF)." *Atmospheric Chemistry and Physics* 9: 1687–1709. doi:10.5194/acp-9-1687-2009.

Staylor, W. F. 1990. "Degradation Rates of the AVHRR Visible Channel for the NOAA 6, 7, and 9 Spacecraft." *Journal of Atmospheric and Oceanic Technology* 70 (3): 411–423. ISSN 1520-0426. doi:10.1175/1520-0426(1990)007<0411:DROTAV>2.0.CO;2.

Sun, B., M. Free, H. L. Yoo, M. J. Forster, A. Heidinger, and K.-G. Karlsson. 2015. "Variability and Trends in U.S. Cloud Cover: ISCCP, PATMOS-x, and CLARA-A1 Compared to Homogeneity-Adjusted Weather Observations." *Journal of Climate* 280 (11): 4373–4389. ISSN 1520-0442. doi:10.1175/JCLI-D-14-00805.1.

Taylor, K. E. 2001. "Summarizing Multiple Aspects of Model Performance in a Single Diagram." *Journal of Geophysical Research: Atmospheres* 1060 (D7): 7183–7192. ISSN 2156-2202. doi:10.1029/2000JD900719.

Theodoridis, S., and K. Koutroumbas. 2008. *Pattern Recognition, Fourth Edition*. 4th ed. Academic Press. ISBN 1597492728, 9781597492720

Urbain, M., N. Clerbaux, A. Ipe, F. Tornow, R. Hollmann, E. Baudrez, A. Velazquez Blazquez, and J. Moreels. 2017. "The CM SAF TOA Radiation Data Record Using MVIRI and SEVIRI." *Remote Sens* 90 (5): 1–31. ISSN 2072-4292. doi:10.3390/rs9050466.

Wielicki, B. A., B. R. Barkstrom, E. F. Harrison, R. B. Lee, G. L. Smith, and J. E. Cooper. 1996. "Clouds and the Earth's Radiant Energy System (CERES): An Earth Observing System Experiment." *Bulletin of the American Meteorological Society* 770 (5): 853–868. ISSN 0003-0007. doi:10.1175/1520-0477(1996)077<0853:CATERE>2.0.CO;2.

Wilson, A. M., B. Parmentier, and W. Jetz. 2014. "Systematic Land Cover Bias in Collection 5 {MODIS} Cloud Mask and Derived Products a Global Overview". *Remote Sensing of Environment* 141: 149–154. ISSN 0034-4257. 10.1016/j.rse.2013.10.025

Zhang, X., M. Friedl, and C. Schaaf. 2006. "Global Vegetation Phenology from Moderate Resolution Imaging Spectroradiometer (MODIS): Evaluation of Global Patterns and Comparison with *in Situ* Measurements." *Journal of Geophysical Reaseach: Biogeosciences* 1110 (G4017): 1–14. doi:10.1029/2006JG000217. ISSN 2169-8961.